International Journal of Fatigue 134 (2020) 105522

Contents lists available at ScienceDirect

International Journal of Fatigue

journal homepage: www.elsevier.com/locate/ijfatigue

Effect of microstructural evolution on the cyclic softening of a 10% Cr martensitic steel under low cycle fatigue at 600 °C

R. Mishnev, N. Dudova*, R. Kaibyshev

Belgorod State University, Belgorod 308015, Russia

ARTICLE INFO

Keywords:
Martensitic steel
Low cycle fatigue
Cyclic softening
Dislocations
Electron microscopy

ABSTRACT

Microstructure evolution and softening during interrupted low cycle fatigue (LCF) tests at 600 °C and constant strain amplitudes of ± 0.2% and ± 0.6% corresponding to dominance of the elastic and plastic strain components, respectively, was examined in a 10% Cr steel. Cyclic softening attributed to changes in the strengthening from dislocations and lath structure is more pronounced during the first half-life. The Burgers vector analysis of dislocation reveals the role of the single and multiple dislocation slip in retention and transformation of lath structure at cycling with low and high strain amplitude, respectively.

1. Introduction

High-chromium martensitic steels are used for critical components of fossil power plants due their superior creep resistance [1,2]. The high creep strength is attributed to the tempered martensite lath structure (TMLS) consisting of a hierarchical sequence of structural elements, i.e., prior austenite grains (PAGs), packets, blocks and laths with a high density of free dislocations [1–3]. The stability of the TMLS is provided by a dispersion of secondary phase particles hindering the transformation of the lath structure into the subgrain structure under creep conditions [1,2,4–10]. Under tempering the $M_{23}C_6$ carbides precipitate at boundaries of structural elements including lath boundaries, and M(C,N) carbonitrides precipitate in the ferritic matrix [1,2,11–13]. In addition, Laves phase particles precipitate during creep [1,2,4–10,14,15].

Low cycle fatigue (LCF) which is caused by cyclic thermal stresses from start-up/shut-down regimes of steam turbines, also induces transformation of the TMLS to the subgrain structure which deteriorates the creep strength [16–24]. High-chromium steels exhibit an extensive softening during cyclic loading at elevated temperatures as a result of evolution of TMLS in the nearly same way as under creep conditions that reduces their service life [16–24]. The main microstructural changes contributing the cyclic softening consist in the decreasing the dislocation density by dislocation annihilation, coarsening of martensitic laths and transformation of lath structure into dislocation cell and subgrain structure [4–10,16–24]. Despite the fact that microstructural evolution leading to cyclic softening is considered in a limited number of works [25,26] the models describing a decrease in the dislocation density and the subgrain coarsening at elevated [23] and room [27] temperatures were developed. In contrast to creep, under LCF conditions the dispersion of secondary-phase particles changes insignificantly. Nevertheless, coarsening of precipitates and their dissolution can decrease the pinning effect on the dislocations and contribute to cyclic softening [17,28].

It is known that the strain amplitude affects significantly the LCF behavior and the transformation processes of the TMLS into the subgrain structure at elevated temperatures [16,18,28]. Thus, cycling of the 10% Cr steel with low strain amplitude in which an elastic strain dominates results in the formation of subgrains of rectangular shape [16]. The crystal lattice retains its orientation and boundary $M_{23}C_6$ carbides restrain the migration of lath/subgrain boundaries. In contrast, during cycling with high strain amplitude the complete transformation of lath structure into subgrain structure occurred and well-defined equiaxed subgrains with re-oriented crystal lattice evolved. The facilitated migration of subgrain boundaries is not impeded by the chains of boundary carbides under these conditions. On the other hand, an increase in the strain amplitude promotes the propagation of fatigue cracks that significantly affects the LCF behavior and fatigue life [16].

To reveal the effect of microstructural changes on the cyclic softening of the 10% Cr steel the microstructural evolution is examined by interrupted LCF tests in relation with a decrease in the microhardness at a temperature of 600 °C.

The 10% Cr steel belongs to a new generation of martensitic steels containing the decreased N and increased B contents and demonstrating an extremely high creep strength at 650 °C due to superior stability of TMLS under creep condition [9,10,29]. The $M_{23}C_6$ carbides in this steel

* Corresponding author.
E-mail addresses: mishnev@bsu.edu.ru (R. Mishnev), dudova@bsu.edu.ru (N. Dudova), rustam_kaibyshev@bsu.edu.ru (R. Kaibyshev).

https://doi.org/10.1016/j.ijfatigue.2020.105522
Received 19 November 2019; Received in revised form 28 January 2020; Accepted 30 January 2020
Available online 31 January 2020
0142-1123/

are characterized by the enhanced coarsening resistance under aging and creep conditions [9–11]. In the same time, LCF behaviors of this steel and the 9–12% Cr steels containing conventional B and N contents are nearly the same [16–21,30–32]. Therefore, the origin of structural degradation under cyclic loading established in the present study will be not only essential for the 10% Cr steel, but also is important for predicting lifetime during LCF tests of other high-chromium steels.

2. Experimental procedure

A 10% Cr steel with the chemical composition (in wt.%) of 0.1% C, 0.06% Si, 0.1% Mn, 10.0% Cr, 0.17% Ni, 0.7% Mo, 0.05% Nb, 0.2% V, 0.003% N, 0.008% B, 2.0% W, 3.0% Co, 0.002% Ti, 0.006% Cu, 0.01% Al and Fe-balance was examined. The steel was subjected to normalizing at 1060 °C for 30 min followed by air-cooling and final tempering at 770 °C for 3 h. Other details of material and processing were reported previously [9,10,11,16,30,31,32].

LCF tests were carried out at 600 °C under fully reversed tension-compression loading conditions with constant total strain amplitudes on cylindrical specimens with a uniform-gauge section length of 18 mm (the distance between the extensometer rods was 12 mm) and a diameter of 5 mm using an Instron 8801 testing machine equipped by the version 8.0 of the Instron LCF 3 software according to ASTM E 606. The temperature of the specimens was controlled during the testing and ΔT did not exceed the required 1%. The ratio of minimum strain to maximum strain was −1 and the frequency was 0.5 Hz. The total strain amplitude was $\varepsilon_{ac} = \pm 0.2\%$ (low) and $\varepsilon_{ac} = \pm 0.6\%$ (high), that were determined to correspond to dominance of either elastic or plastic strain components in the total strain amplitude, respectively, in previous works [30,31]. First, the LCF tests up to failure were carried out which were stopped when the stress amplitude decreased by more than 20% over the last 50 cycles. Stress–strain hysteresis loops were recorded continuously to determine the cycle-dependent changes in the stress and plastic strain amplitude. Then, the interrupted at different stages LCF tests were carried out using the subsequent specimens, one specimen per one level. The interruptions were made at the onset of softening stage (after 5 and 30 cycles), at half-life stage (after 9000 and 500 cycles) at $\varepsilon_{ac} = \pm 0.2\%$ and at $\varepsilon_{ac} = \pm 0.6\%$, respectively. The interrupted tests were stopped after a full loop closing cycles using the Instron LCF 3 software. The microhardness was determined using a Wilson Wolpert 402 MVD hardness tester under a load of 300 g on the samples subjected to mechanical and electro-polishing with an accuracy of 4%.

The microstructure was examined using a Quanta 600FEG scanning electron microscope equipped with electron backscatter diffraction (EBSD) pattern analyzer incorporating an orientation imaging microscopy (OIM) system and a JEOL JEM-2100 transmission electron microscope (TEM). TEM foils were prepared by double-jet electro-polishing using a solution of 10% perchloric acid in glacial acetic acid. OIM images were obtained with a step size of 120 to 170 nm and subjected to a cleanup procedure, establishing a minimal confidence index of approximately 0.1 and a minimal number of points per grain of 8. High- and low-angle boundaries (HABs and LABs) were defined to have a misorientation of ≥15° and 2° ≤ θ < 15° and depicted in the OIM maps using black and white lines, respectively. In order to evaluate the distribution of strain or the stored energy in TMLS the kernel average misorientation (KAM) values were obtained from OIM images. The transverse lath/subgrain sizes were measured on the TEM micrographs by the linear intercept method, counting all the clear visible (sub) boundaries. The dislocation densities were estimated by counting the individual dislocations in the (sub)grain/lath interiors per unit area on at least six arbitrarily selected typical TEM images for each data point. The equilibrium volume fractions of phases were calculated by version 5 of the Thermo-Calc software using the TCFE7 database entering the BCC A2, FCC A1, M23C6 and Laves phase C14 equilibrium phases for the actual steel composition.

3. Results

3.1. Microstructure after normalization and tempering

Fig. 1 shows TMLS of the 10% Cr steel. It was described in detail previously [9,10,11,16,30,31,32]. An average size of PAGs is ~35 μm, average thickness of laths is ~0.4 μm; and the dislocation density within the lath interiors is $\sim 1.7 \times 10^{14}$ m^{-2}. The main feature of TMLS of the 10% Cr steel is the presense of coarse laths having low continuous misorientions along with blocks exhibiting high continuous misorientations (Fig. 1a). The internal distortions is predominantly localized in blocks, whereas coarse laths are almost strain-free (Fig. 1b). Therefore, the packets of TMLS consist of two structural components distinctly distinguished by internal stress fields. $M_{23}C_6$ carbides with an average size of about 70 nm densely locate at HABs of PAGs, packets, and low-angle lath boundaries in nearly equal proportions, although some lath boundaries are almost free of these carbides. Nb(C,N) carbonitrides with a size of 30 nm are uniformly distributed within the martensite laths.

3.2. Fatigue behavior

The LCF curves for the 10% Cr steel at 600 °C are shown in Fig. 2. Fatigue life decreases from 17,213 to 954 cycles with an increase in the strain amplitude, ε_{ac}, from ± 0.2% to ± 0.6%. At $\varepsilon_{ac} = \pm 0.2\%$, the steady-state stage is observed during the first 40 cycles followed by a continuous cyclic softening with a coefficient of $\Delta\sigma/\Delta \lg N_f = 22$. At $\varepsilon_{ac} = \pm 0.6\%$, the onset of cyclic softening is characterized by $\Delta\sigma/\Delta \lg N_f = 44$, it appears immediately after the first cycle and takes place up to failure. Therefore, increasing the strain amplitude leads to two-fold increase in the softening coefficient.

Fig. 3 demonstrates the effect of number of reversals on hysteresis loops. The symmetric profiles for the first cycle loop that are typical for

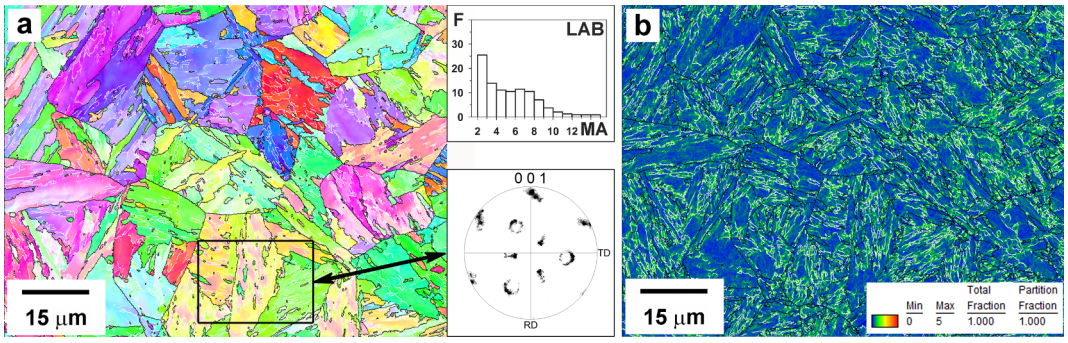

Fig. 1. Structure of the 10% Cr steel in normalized-and-tempered condition: (a) OIM image with corresponding {0 0 1} pole figure and distribution of LABs misorientation; (b) KAM map.

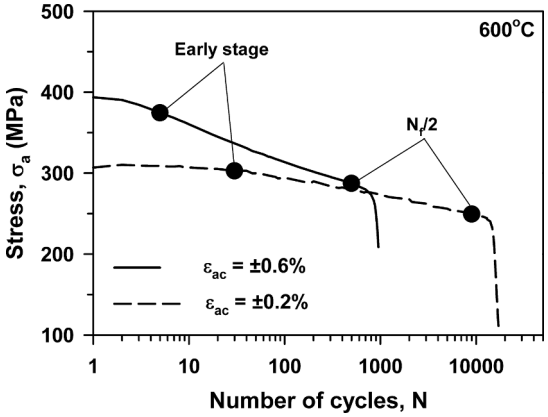

Fig. 2. Cyclic stress response curves of the 10% Cr steel at 600 °C. Filled circle symbols indicate the points, where the fatigue tests were interrupted for microstructure characterization.

strain softening [32] are observed. At ε_{ac} = ± 0.2%, the plastic strain component ε_{ap} = ± 0.0272% that comprises 13.6% from the total strain amplitude after 30 cycles and these value increases by more than 2 times at half-life cycles (Fig. 3a and c, Table 1). At ε_{ac} = ± 0.6%, the contribution of plastic strain comprises 59% after the first cycle and slightly increases with an increase in the number of cycles to half-life cycles (Fig. 3b and c, Table 1). The stress amplitude decreases during LCF testing due to cyclic softening. Therefore, the second half-life cycles are charactarized by the significantly higher plastic strains than the first half-life cycles. A difference in the contribution of plastic strain to overall strain amplitude between the first and second half-life cycles is more pronounced at ε_{ac} = ± 0.2% than at ε_{ac} = ± 0.6%.

3.3. Microhardness evolution under LCF at 600 °C

Microhardness of the 10% Cr steel in the tempered condition is 240 HV (Fig. 4, Table 2). The microhardness change during cyclic deformation at 600 °C is shown in Fig. 4. The steel demonstrates similar decrease (on approximately 2–3%) in the microhardness after 30 and 5 cycles at strain amplitudes of ± 0.2 and ± 0.6%, respectively. Further cyclic loading up to failure leads to a gradual decrease in the microhardness down to 220 and 215 HV at strain amplitudes of ± 0.2 and ± 0.6%, respectively. At the half-life stage (9000 and 500 cycles), the microhardness reduces to 224 and 220 HV at low and high ε_{ac}, respectively (Table 2). Therefore, microhardness decreases mainly in the first half of the life-time on approximately 7% and 9% as compared to the initial state for ε_{ac} = ± 0.2% and ε_{ac} = ± 0.6%, respectively (Table 2, Fig. 4). In contrast, the following half of cycling leads to an additional 1–1.5% decrease in microhardness. The fractured samples after LCF tests with low and high strain amplitudes are characterized by relatively high level of microhardness, respectively, which comprises 92% and 90% from the initial microhardness, respectively.

3.4. Microstructure evolution under LCF at 600 °C

Evolutions of the TMLS under dominance of the elastic (ε_{ac} = ± 0.2%) and plastic (ε_{ac} = ± 0.6%) strain amplitudes are distinctly different (Figs. 5–9).

At the onset of the softening stage after 30 cycles at ε_{ac} = ± 0.2% and after 5 cycles at ε_{ac} = ± 0.6%, the rearrangment and partial annihilation of lattice dislocations leads to a decrease in the dislocation density by 6% and 24%, respectively (Fig. 5a and b, 6a and b, 9). As a result, a slight increase in the fraction of LABs with misorientation of 2° and 6° appears (Fig. 5a and b, Table 2). At ε_{ac} = ± 0.6%, a 20%

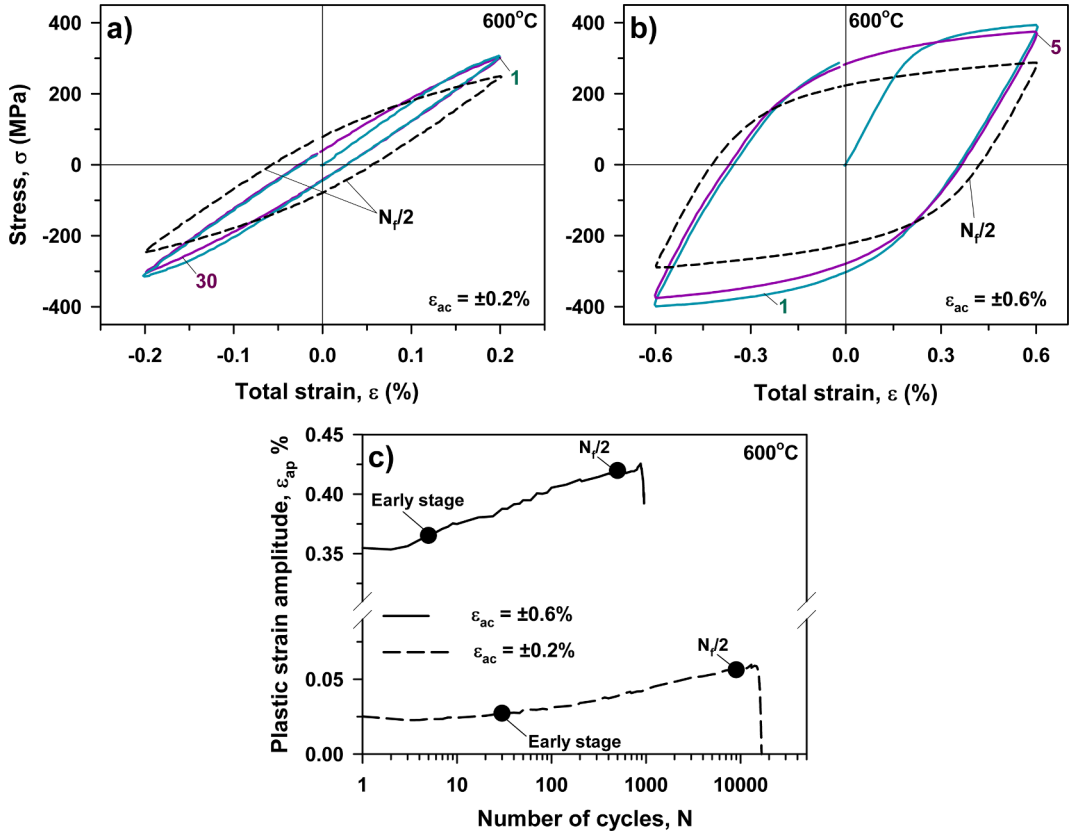

Fig. 3. Stress-strain hysteresis loops of the 10% Cr steel for cycles ranging from first to half-life at ε_{ac}: (a) ± 0.2%, (b) ± 0.6%. Effect of number of cycles at strain amplitudes ε_{ac} = ± 0.2% and ε_{ac} = ± 0.6% on the plastic strain amplitude (c).

Table 1
Change in the low cycle fatigue data at 600 °C of the 10% Cr steel with number of cycles.

Number of cycle	ε_{ac} = ± 0.2%				ε_{ac} = ± 0.6%			
	1	30	9000	13,000	1	5	400	700
ε_{ap}, %	0.0256	0.0272	0.0564	0.0589	0.3552	0.3665	0.4172	0.4229

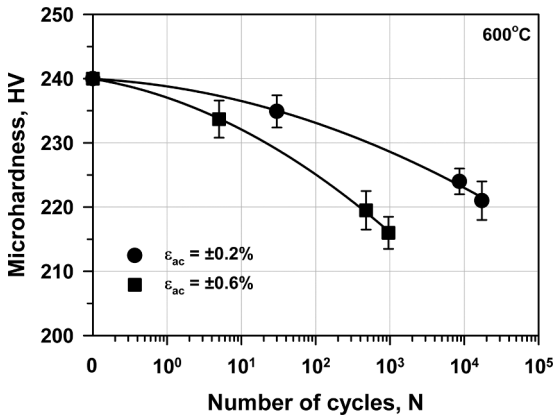

Fig. 4. Effect of number of cycles at strain amplitudes ε_{ac} = ± 0.2% and ± 0.6% on the microhardness.

Table 2
Microhardness and microstructural parameters after fatigue tests at 600 °C interrupted at different stages. Numerator and denominator are values measured at ε_{ac} = ± 0.2% and ε_{ac} = ± 0.6%, respectively.

Before tests	Early stage (30/5) cycles	Half-life (9000/500) cycles	Failured (17213/954) cycles
		Microhardness, HV	
240.0	234.9/233.7	224.0/219.5	221.0/216.0
		Lath width, nm	
400	410/490	580/680	580/-
		Subgrain size, nm	
390	320/470	410/590	500/900
		Dislocation density, $\times 10^{14}$ m^{-2}	
1.70	1.60/1.30	1.30/0.80	1.20/0.58
		Fraction of LAB, %	
58.1	50.7/53.6	53.9/49.4	54.4/50.2
		Portion of LABs with misorientation of 2°, %	
25	27/27	27/25	30/24
		Portion of LABs with misorientation of 4-6°, %	
31	38/37	36/40	32.5/36
		Density of LABs, $\times 10^{5}$ m^{-1}	
10	6.8/6.3	6.5/5.8	8.1/7.3
		Density of HABs, $\times 10^{5}$ m^{-1}	
7	6.6/5.5	5.5/6.0	6.7/7.3

increase in the mean lath width accompanied by a significant decrease in the lattice dislocation density occurs that is in contrast to ε_{ac} = ± 0.2%, where the lath width remains unchanged and the subgrains having rectangular shape and bounded by LABs appear due to subdivision of laths by transverse LABs (Fig. 6a and b). Therefore, the cyclic loading with dominance of the plastic strain amplitude leads to the significant microstructural changes even after 5 cycles.

At the half-life cycles corresponding to the middle of the softening stage, the different TMLSs evolve after cyclic loading at the low and high strain amplitudes. At ε_{ac} = ± 0.2%, a loading for 9000 cycles leads to the 45% increase in the lath width and 24% decrease in the lattice dislocation density (Figs. 6c and d, 9). The TMLS does not significantly change as suggested by well-defined "Bain circles" indicating of absence of significant re-orientation of the crystal lattice under cyclic loading (Fig. 5c). Also, the high continuous misorientations associated with the internal stresses remain in the most of packets; an insignificant relief of the internal stresses occurs in blocks with initially high continuous misorientation (Fig. 5c). The chains of carbides effectively pin the lath boundaries preventing their migration (Fig. 6c and e). On the other hand, the rearrangment of dislocations comprising the lath boundaries which are almost free of carbides leads to the transformation of these lath boundaries into subboundaries and their migration resulting in a decrease in the density of LABs (Fig. 6c, Table 2) [30,31]. As a result, the subgrain structure with the mean subgrain size of 410 nm evolved in the lath interiors, while the coarse subgrains with dimensions ranging 0.5…2.5 μm form in the coarse laths (Fig. 7a).

At ε_{ac} = ± 0.6%, the main feature of microstructural evolution at the half-life cycles is the detachment of some lath boundaries from particles (Fig. 6d and f). An ability of particles to pin the lath boundaries tends to decrease with increasing the plastic strain amplitude. As a result, at ε_{ac} = ± 0.6%, the microstructural changes are more pronounced than at ε_{ac} = ± 0.2% despite the fact that the number of half-life cycles of N = 500 at ε_{ac} = ± 0.6% is less by an order of magnitude than that at ε_{ac} = ± 0.2%. The increase in the lath width by 70% and decrease in the lattice dislocation density by 53% occur in comparison with the tempered condition (Fig. 9, Table 2). A major part of lath boundaries transforms to the subboundaries which exhibit the extinction fringes (Figs. 5d, 6d and f). Nevertheless, the lath structure retains that is confirmed by the retention of the "Bain circles" on {0 0 1} pole figures as well as the internal stress fields on the KAM map (Fig. 5d). The density of LABs is less than that at ε_{ac} = ± 0.2% (Table 2) indicating of the strain-induced coalescence of subgrains that leads to a larger size of subgrains (Figs. 7b, 9b, Table 2). A decrease in the internal stresses with increasing number of loading cycles is seen in the KAM map (Fig. 5d and f). Therefore, the transformation of the lath boundaries to the subgrain boundaries followed by their migration within blocks having initially high continuous misorientation relives an internal stress and increases the number of coarse laths/subgrains with low internal distortions, although this process occurs with a low rate during the first half-life cycles.

Further cyclic loading up to failure pronounces the difference in the effect of strain amplitudes on the microstructure. At ε_{ac} = ± 0.2%, any significant changes in TMLS hardly occur during the second half of the fatigue test. The mean width of laths and lattice dislocation density remain essentially the same (Fig. 8a, Table 2). The lath boundaries and lattice dislocations are effectively pinned by densely distributed $M_{23}C_6$ carbides and M(C,N) particles [4,5,9–12]. The mean subgrain size continuously increases up to 500 nm (Table 2). Scarce dislocation glide attributed to a low strain amplitude leads to an insignificant decrease in the dislocation density down to ~1.2 × 10^{14} m^{-2} and retains the crystallite orientations during the second half of fatigue test (Fig. 5e, 9a, Table 2). Areas of blocks remain misorientated (Fig. 5e), while TEM micrographs show an evidence for relieving the stress fields originated from lath boundaries (Fig. 8a). Thus, an elastic strain provides the redistribution of lattice dislocations from lath interiors to lath boundaries and rearrangement of intrinsic dislocations comprising these boundaries into the low-energy configurations (Fig. 8a). As a result, the fraction of LABs with misorientation of 2° increases up to 30% along with increasing the LAB density (Table 2). The knitting reaction between free dislocations and dislocations of lath boundaries occurs with a low rate and leads to an insignificant mutual annihilation.

In contrast, at ε_{ac} = ± 0.6%, the transformation of the lath boundaries into the subboundaries is assisted by frequent knitting

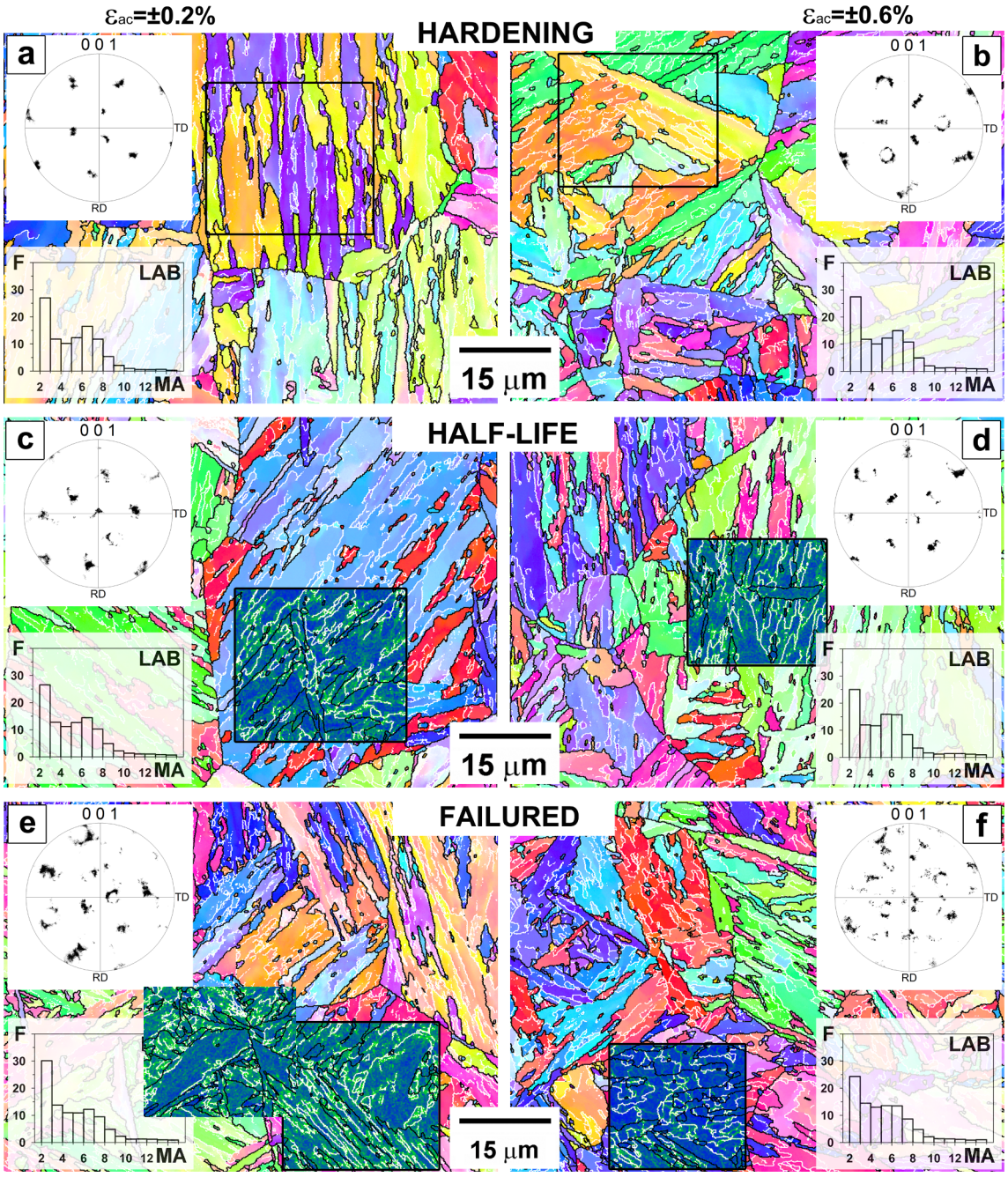

Fig. 5. OIM images with corresponding {0 0 1} pole figure, distribution of LABs misorientation and KAM maps of the 10% Cr steel after fatigue tests at 600 °C ε_{ac} = ± 0.2% (a,c,e) and ε_{ac} = ± 0.6% (b,d,f), interrupted at different stages (indicated on images).

reaction leading to a three-fold decrease in the density of lattice dislocations (Table 2, Fig. 9a). This transformation is completed during the second life-time cyclic loading. A high plastic strain amplitude [31] provides the formation of the coarse subgrain structure with the mean subgrain size of 0.9 μm in the whole material volume (Figs. 5f, 8b). The KAM values remarkably decrease in the interiors of packets and individual PAGs (Fig. 5f). The migration of subgrain boundaries during the second life-time cycles appears at the level of packets. The partial spreading of "Bain circles" and appearance of numerous diffused spots on a {0 0 1} pole figure (Fig. 5f) are indicative of re-orientation of the lattice due to dislocation glide. This spreading correlates with the replacement of laths by subgrains. The fraction of LABs with misorientation of about 6° increases (Fig. 5f, Table 2) whereas that of 2° decreases along with an increase in the dimensions of crystallites outlined by LABs. These changes evidence for the accumulation of subboundary misorientation.

Therefore, the main difference in the evolutions of the TMLS during cyclic loading with dominance of the elastic or plastic strain amplitudes is attributed to different rate of the knitting reaction between lattice dislocations and dislocations comprising lath boundaries. This reaction leads to the partial transformation of lath boundaries to subgrain boundaries during the second half-life cycles at ε_{ac} = ± 0.2%, whereas the major portion of lath boundaries transform to subgrain boundaries during the first half-life cycles at ε_{ac} = ± 0.6%. Boundary carbides are effective in the pinning of lath boundaries and non-effective in the pinning of subgrain boundaries. Migration of the lath boundaries is arrested by precipitates up to failure and only lath boundaries, which were almost free of carbides, are able to migrate that leads to an

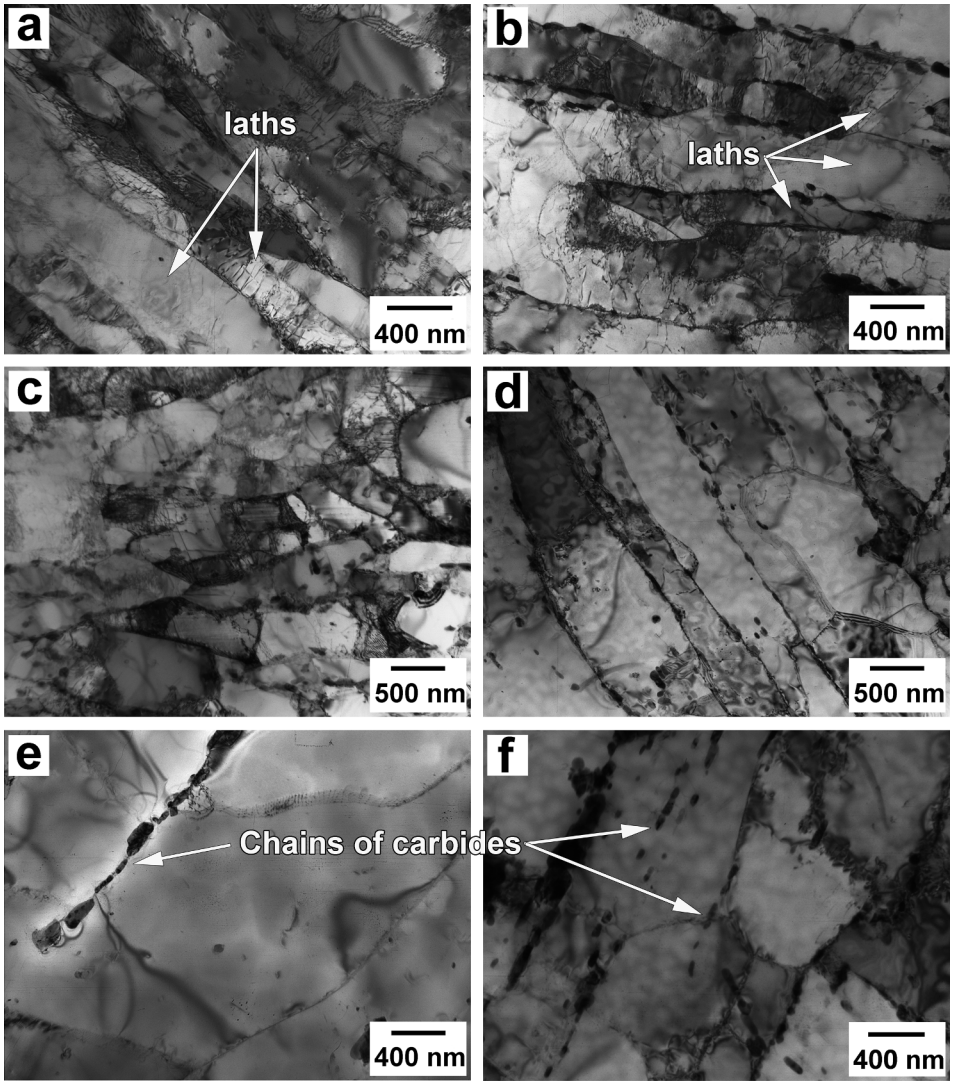

Fig. 6. TEM micrographs of the 10% Cr steel after fatigue tests with $\varepsilon_{ac} = \pm 0.2\%$ (a,c,e) and $\varepsilon_{ac} = \pm 0.6\%$ (b,d,f), interrupted at the onset of softening stage: a) $\varepsilon_{ac} = \pm 0.2\%$, $N = 30$ cycles and b) $\varepsilon_{ac} = \pm 0.6\%$, $N = 5$ cycles; and half-life stage: c,e) $\varepsilon_{ac} = \pm 0.2\%$, $N = 9000$ cycles and d,f) $\varepsilon_{ac} = \pm 0.6\%$, $N = 900$ cycles.

increase in the lath width at $\varepsilon_{ac} = \pm 0.2\%$. At $\varepsilon_{ac} = \pm 0.6\%$, the detachment of subgrain boundaries from $M_{23}C_6$ carbides at the second half-life cycles yields an extensive migration of these boundaries.

4. Discussion

4.1. Relation between microhardness and microstructural parameters

Fig. 10a shows a decrease in the microhardness H/H_0 as a function of fatigue life fraction N/N_f. It is seen that microhardness decreases more intensively during the first half of the life-time than during the second one. This finding is evidenced by approximately 4 times larger the slope of H/H_0 *vs* N/N_f curves at the first half of cycling (Fig. 10a). The rate of microhardness decrease at first half-life is about 30% higher for a high strain amplitude as compared with a low strain amplitude, whereas at the second half it is nearly the same for both strain amplitudes.

It is known that a decrease in the hardness under creep conditions is related to creep life fraction as the follows [33,34]:

$$t/t_R = (1/0.15) \times (0.98 - H_t/H_o) \quad (1)$$

where t_R is the rupture time and t is the certain creep time. This equation allows predicting remnant life time in high-chromium steels with a high accuracy [4,33,34].

According to Fig. 10a, a decrease in microhardness of the 10% Cr steel under LCF condition can be expressed by the following relation:

$$H/H_0 = 0.98 - k(N/N_f) \quad (2)$$

where coefficient k varies from 0.09 to 0.12 depending on the strain amplitude ($\varepsilon_{ac} = \pm 0.2\%$ and $\varepsilon_{ac} = \pm 0.6\%$, respectively) and the mean k is 0.11. However, this dependence is actual only for the first half-life because a decrease in microhardness is insignificant during the second half-life.

In order to reveal the effect of microstructural changes on the softening of steel under fatigue condition, let us consider the change in the square root dislocation density $\sqrt{\rho}$ and inverse lath width $1/d_{lath}$ as a function of fatigue life fraction N/N_f (Fig. 10b and c). These values are known to determine the strengthening factors from free dislocations ΔH_{disl} and substructure ΔH_{lath}, which correlates linearly to strength $\Delta\sigma_{disl}$ and $\Delta\sigma_{lath}$, respectively, according to the following relationships [35]:

$$\Delta H_{disl} \sim \Delta\ \sigma_{disl} = \alpha_1 MGb\sqrt{\rho} \quad (3)$$

$$\Delta H_{lath} \sim \Delta\ \sigma_{lath} = \alpha_2 Gb/d_{lath} \quad (4)$$

where α_1 and α_2 are the material constants, M is the Taylor factor, G is the shear modulus, b is the Burgers vector.

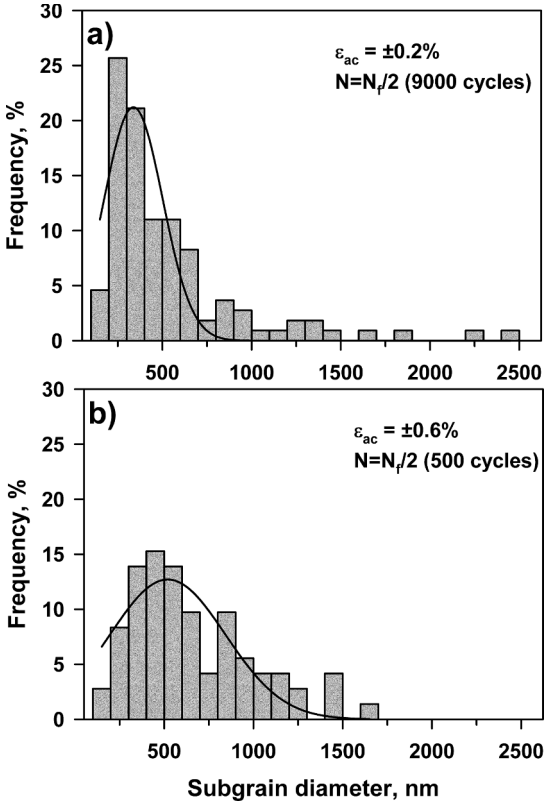

Fig. 7. Distribution of subgrain diameter measured at the half-life stage of fatigue tests with $\varepsilon_{ac} = \pm 0.2\%$ (a) and $\varepsilon_{ac} = \pm 0.6\%$ (b).

The onset of cyclic softening (30 and 5 cycles) at the low and high strain amplitude is characterized by the 3% and 13% decrease in $\sqrt{\rho}$ value and 7% and 23% decrease in the $1/d_{lath}$ value, respectively (Fig. 10b and c). However, although these changes differ by 3–4 times for $\varepsilon_{ac} = \pm 0.2\%$ and $\varepsilon_{ac} = \pm 0.6\%$, a decrease in the microhardness is nearly the same for both strain amplitudes and comprises 2–3%. An insignificant microhardness decrease is probably attributed to retention of lath structure.

During the following cycling up to the half-life cycles, the rate of decreasing the square root dislocation density estimated by the slope of $\sqrt{\rho}$ *vs* N/N_f curve is 2 times higher at a high strain amplitude than that at a low strain amplitude (Fig. 10b). On the other hand, the lath width parameter ($1/d_{lath}$) decreases with the similar rate at both strain amplitudes up to half-life (Fig. 10c). Therefore, a 1.3 times higher the rate of microhardness decrease at a high strain amplitude during the first half-life is obviously attributed to a 2 times higher the rate of decreasing the $\sqrt{\rho}$ value. It can be suggested that a decrease in the strengthening factor from dislocation density due to intensive dislocation annihilation affects the cyclic softening more remarkably than the lath widening during the first half-life.

At the second half-life cycles, approximately 4 times lower the rate of microhardness decrease is accompanied by an approximately 2 times lower the rate of $\sqrt{\rho}$ decrease as well as lower changes in the inverse size of lath or subgrains (for $\varepsilon_{ac} = \pm 0.6\%$) (Fig. 10). So, changes in the strengthening from free dislocations and lath structure is more pronounced during the first half-life. This finding is in accordance with the results on the other 9%Cr martensitic steels [25,27]. The lower softening rate at the second half of cyclic testing is probably attributed to the fact that absorbed energy is mainly spent on the fatigue crack propagation at this stage.

On the other hand, the microhardness behavior during the second half-life at the low and high strain amplitudes does not correlate with different changes in the dislocation density and lath width (Fig. 10). Namely, at a low strain amplitude, despite the slight changes in $\sqrt{\rho}$ and $1/d_{lath}$ values the same rate of a microhardness decrease occurs similar to that at a high strain amplitude. It can be suggested that this fact is attributed to a decrease in the solid solution strengthening due to the Laves phase precipitation and depletion of W and Mo from the ferritic matrix. The duration of LCF test at $\varepsilon_{ac} = \pm 0.2\%$ up to failure is approximately 10 h in contrast to short-term (~0.5 h) LCF test at $\varepsilon_{ac} = \pm 0.6\%$. The precipitation of Laves phase is known to be the thermally-activated and not the strain-induced process [36]. So, the several hours of exposition at 600 °C can be enough for starting the precipitation of fine Laves phase particles. As predicted by Thermo-Calc, the volume fraction of Laves phase in the 10%Cr steel at 600 °C is

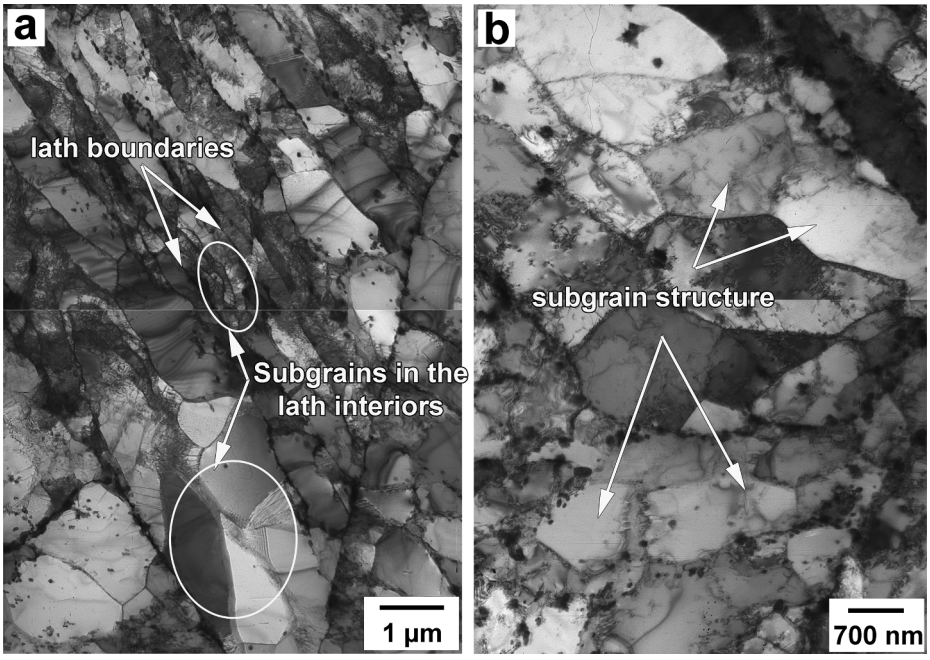

Fig. 8. TEM micrographs of the 10% Cr steel after fatigue failure tests with $\varepsilon_{ac} = \pm 0.2\%$ (N_f = 17 213 cycles) (a) and $\varepsilon_{ac} = \pm 0.6\%$ (N_f = 954 cycles) (b).

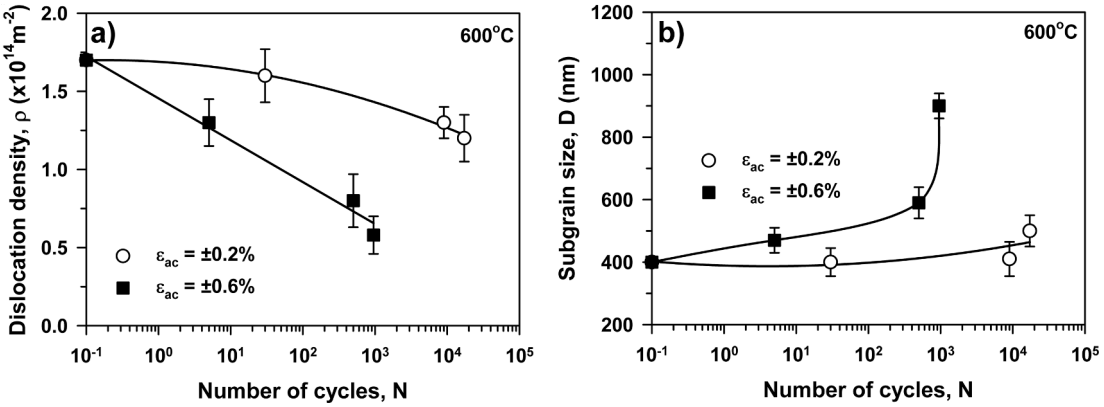

Fig. 9. Effect of number of cycles at strain amplitudes ε_{ac} = ± 0.2% and ε_{ac} = ± 0.6% on the dislocation density (a) and subgrain size (b).

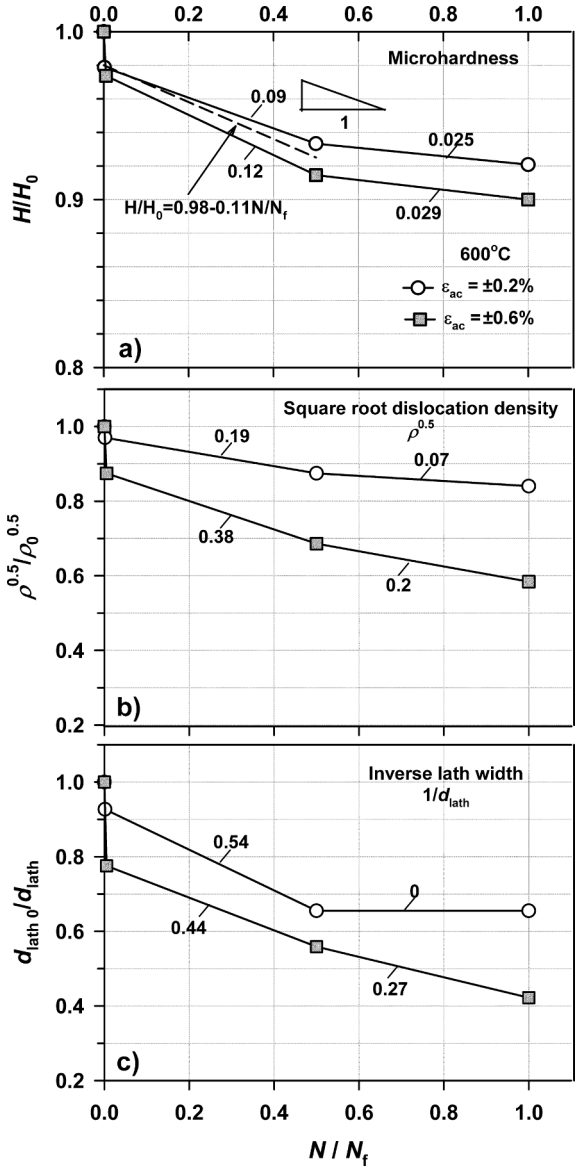

Fig. 10. Change in the microhardness (a), square root dislocation density (b) and inverse lath width (c) *vs* the fatigue life fraction N/N_f at strain amplitudes ε_{ac} = ± 0.2% and ε_{ac} = ± 0.6%.

1.94% whereas Laves phase is not present in the tempered at 770 °C condition. Therefore, the depletion of W and Mo from the ferritic matrix during the cycling with ε_{ac} = ± 0.2% for several hours can contribute to the cyclic softening and result in more significant microhardness decrease despite the insignificant changes in the dislocation density and lath width.

4.2. Burgers vector analysis of dislocations

Suggesting that different rate of knitting reaction determines the significant difference of TMLS evolution during the low- and high-strain amplitude cycling, we considered the dislocation substructure formed at the half-life cycle at a low strain amplitude (N = 9000 cycles, ε_{ac} = ± 0.2%) and at the onset of the softening stage at a high strain amplitude (N = 5 cycles, ε_{ac} = ± 0.6%). It should be noted that the parameters of lath structure such as the mean lath width and subgrain size, dislocation density, fraction and density of LABs (Figs. 5b and c, 6b and c, 9, Table 2) are almost the same in these two conditions as well as carbides are densely distributed on the lath boundaries in both cases.

Burgers vector analysis of dislocations was carried out by means of two-beam condition TEM tecnhique [37]. The dislocations are invisible with the (123) reflection, whereas several dislocations (marked by circles in Fig. 11a) are visible with the $(\bar{2}\bar{1}\bar{1})$ reflection. The same Burgers vector for all the dislocations observed may suggest that the single slip system is operative upon cyclic loading with a low strain amplitude at the half-life cycle, although cross-slip easily occurs in bcc metals/alloys [38].

In contrast, the dislocations of different slip systems are observed at the onset of softening stage at a high strain amplitude. Fig. 11b shows that numerous dislocations are visible with the $(2\bar{1}\bar{1})$ reflection (the left picture) and $(\bar{1}21)$ reflection (the right picture). It is clearly seen that some of dislocations (marked by circles) are only visible with either $(\bar{2}\bar{1}\bar{1})$ or $(\bar{1}21)$ reflections. Therefore, at least two dislocation families with Burgers vectors of $\frac{1}{2}$a $[11\bar{1}]$ and $\frac{1}{2}$a [111] are observed. It is worth noting that almost all LABs consist of two families of dislocations with different Burgers vectors. Therefore, the interaction of dislocations with lath boundaries during cyclic loading with a high strain amplitude may lead to the rapid rearrangement and anihilation of lath boundary dislocations, promoting the transformation of the lath boundaries into the ordinary dislocation subboundaries.

4.3. Microstructural evolution

So, the single slip and multiple slip determines, respectively, the rate of knitting reaction at cycling with the dominance of elastic and

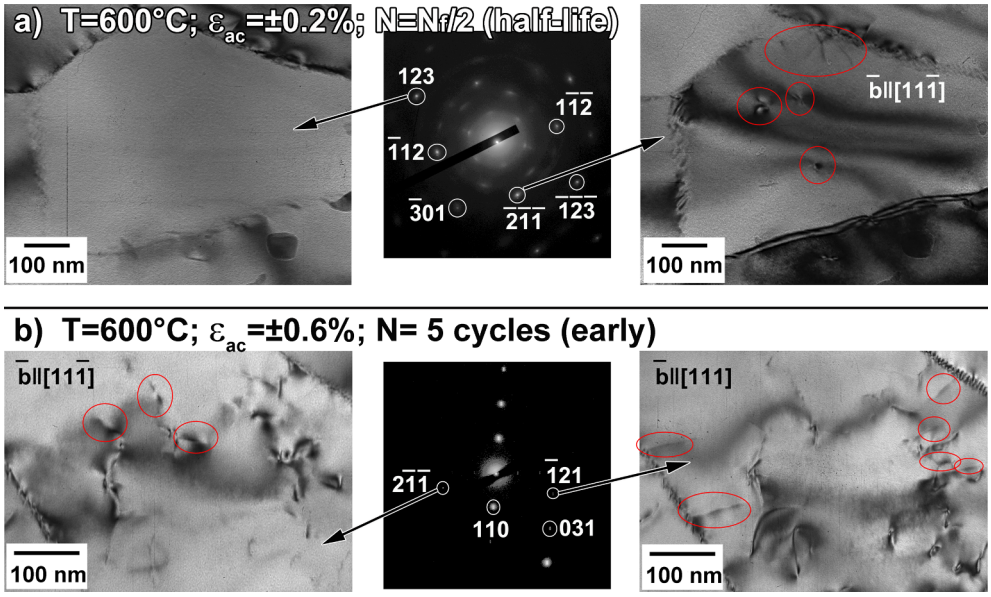

Fig. 11. Bright-field TEM micrographs showing dislocation Burgers vector analysis with dislocations imaged under different beam conditions in the 10% Cr steel after fatigue failure tests: (a) ε_{ac} = ± 0.2%, N = 9 000 cycles; (b) ε_{ac} = ± 0.6%, N = 5 cycles.

plastic strain component. The microstructural evolution during cyclic loading at elevated temperature can be schematically presented as follows (Fig. 12).

At first cycles corresponding to the onset of the softening stage, the dislocations are arranged across the laths due to the reactions between the existing dislocations in the lath interiors and new generated dislocations. Thermal recovery prevents accumulation of dislocations unlike to cyclic deformation at room temperature, where cyclic hardening was observed [32]. Dislocation slip on several systems facilitates knitting reaction at a high strain amplitude that leads to the lower dislocation density and larger lath width than at a low strain amplitude. Operation of only single slip in latter case at the onset and in the middle of the softening stage significantly retards the knitting reaction. As a result, at half-life cycles lath boundaries mainly retain the high internal stress fields. The densely distributed carbides pinning the lath boundaries play the major role in the retention of lath structure at a low strain amplitude. The rearrangment of dislocations comprising lath boundaries leads to the transformation of these boundaries to the subgrain boundaries [30,31]. Subgrain structure evolves in the lath interiors.

In contrast, operation of multiple slip almost eliminates the pinning of lath boundaries by $M_{23}C_6$ carbides and decreases the dispersion hardening in fatigue resistance at high strain amplitude. Therefore, lath

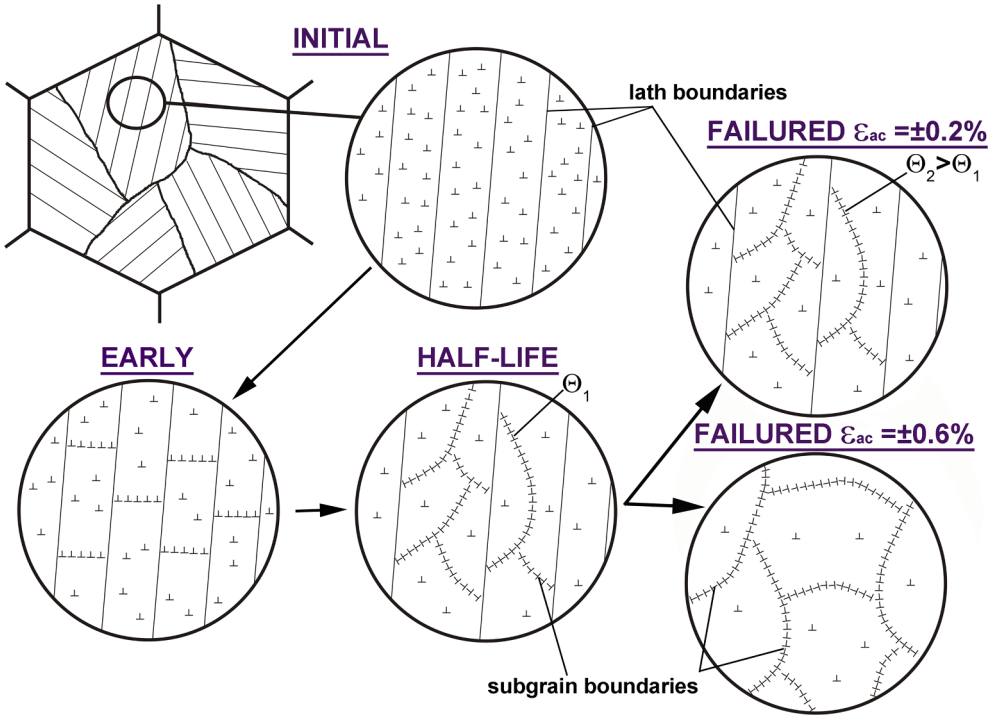

Fig. 12. Schematically presented evolution of microstructure in the 10% Cr steel during LCF test at 600 °C.

structure with the migrating or dissolving boundaries appears at the half-life cycle that is completely replaced by the coarse subgrains during the second half life-time of cyclic loading. Unlike, the lath structure which was formed at half-life cycles retains during the second half of testing up to failure at a low strain amplitude. The mean size of subgrains in the lath interiors and misorientation of their boundaries continuously increase that is attributed to the fact that subgrain boundaries play a role of sources and sinks for lattice dislocations [39,40].

5. Conclusions

In this work, we examined the microhardness and microstructural evolution during the interrupted low cycle fatigue (LCF) tests with the low and high strain amplitudes of ± 0.2% and ± 0.6%, corresponding to dominance of the elastic and plastic strain components, respectively, at elevated temperature of 600 °C in a 10% Cr-2% W-0.7% Mo-3% Co-0.05% Nb-0.2% V-0.008% B-0.003% N steel (all in wt.%). The main results are summarized as follows:

1. At the onset of the softening stage after 30 and 5 cycles at the low and high strain amplitudes, respectively, a similar slight decrease in microhardness of 2 and 3% occurs due to retention of lath structure despite a 3–4 times higher decrease in the strengthening from dislocation density and lath structure at a high strain amplitude.
2. The rate of microhardness decrease during the first half-life is approximately 4 times higher than during the second half-life that is accompanied by the higher rate of a decrease in the strengthening from dislocations and lath structure. During the first half-life, the lath structure retains independently of strain amplitude, while a higher strain amplitude provides a 30% higher rate of microhardness decrease due to a 2 times higher rate of decreasing the strengthening from dislocation density.
3. During the second half-life, transformation of the lath boundaries to the subboundaries is completed at cycling with a high stain amplitude. The depletion of W and Mo from the ferritic matrix during the cycling with a low strain amplitude can contribute to the cyclic softening and result in more significant microhardness decrease despite the insignificant changes in the dislocation density and lath width.
4. At a low strain amplitude, an operation of mainly single dislocation slip provides the retention of pinning of lath boundaries by $M_{23}C_6$ carbides that retards the transformation of the lath structure into a subgrain structure up to rupture.
5. At a high strain amplitude, the multiple slip occurring starting at the onset of the softening stage almost eliminates the pinning of lath boundaries by $M_{23}C_6$ carbides that facilitates the transformation of the lath structure into a subgrain structure.

Declaration of Competing Interest

The authors declare that they have no known competing financial interests or personal relationships that could have appeared to influence the work reported in this paper.

Acknowledgments

This study was financial supported by the Russian Science Foundation, Russian Federation, under grant No. 19-79-00195. The authors are grateful to Dr. A. Belyakov, Belgorod State University, for fruitful discussion of results. The authors are grateful to the staff of the Joint Research Center, “Technology and Materials”, Belgorod State University, for providing the equipment for instrumental analysis.

References

[1] Abe F, Kern T-U, Viswanathan R. Creep-resistant steels. Cambridge: Woodhead Publishing Limited; 2008. p. 678.
[2] Kaybyshev RO, Skorobogatykh VN, Shchenkova IA. New martensitic steels for fossil power plant: creep resistance. Phys Met Metall 2010;109:186–200. https://doi.org/10.1134/S0031918X10020110.
[3] Kitahara H, Ueji R, Tsuji N, Minamino Y. Crystallographic features of lath martensite in low-carbon steel. Acta Mater 2006;54:1279–88. https://doi.org/10.1016/j.actamat.2005.11.001.
[4] Fedoseeva A, Dudova N, Kaibyshev R. Creep strength breakdown and microstructure evolution in a 3%Co modified P92 steel. Mater Sci Eng A 2016;654:1–12. https://doi.org/10.1016/j.msea.2015.12.027.
[5] Dudko V, Belyakov A, Molodov D, Kaibyshev R. Microstructure evolution and pinning of boundaries by precipitates in a 9 pct Cr heat resistant steel during creep. Metall Mater Trans A 2013;44:162–72. https://doi.org/10.1007/s11661-011-0899-1.
[6] Kipelova A, Kaibyshev R, Belyakov A, Molodov D. Microstructure evolution in a 3%Co modified P911 heat resistant steel under tempering and creep conditions. Mater Sci Eng A 2011;528:1280–6. https://doi.org/10.1016/j.msea.2010.10.006.
[7] Kostka A, Tak KG, Hellmig RJ, Estrin Y, Eggeler G. On the contribution of carbides and micrograin boundaries to the creep strength of tempered martensite ferritic steels. Acta Mater 2007;55:539–50. https://doi.org/10.1016/j.actamat.2006.08.046.
[8] Abe F. Analysis of creep rates of tempered martensitic 9%Cr steel based on microstructure evolution. Mater Sci Eng A 2009;510–511:64–9. https://doi.org/10.1016/j.msea.2008.04.118.
[9] Mishnev R, Dudova N, Fedoseeva A, Kaibyshev R. Microstructural aspects of superior creep resistance of a 10%Cr martensitic steel. Mater Sci Eng A 2016;678:178–89. https://doi.org/10.1016/j.msea.2016.09.096.
[10] Mishnev R, Dudova N, Kaibyshev R. On the origin of the superior long-term creep resistance of a 10% Cr steel. Mater Sci Eng A 2018;713:161–73. https://doi.org/10.1016/j.msea.2017.12.066.
[11] Dudova N, Mishnev R, Kaibyshev R. Effect of tempering on microstructure and mechanical properties of boron containing 10% Cr steel. ISIJ Int 2011;51:1912–8.
[12] Fedorova I, Kostka A, Tkachev E, Belyakov A, Kaibyshev R. Tempering behavior of a low nitrogen boron-added 9%Cr steel. Mater Sci Eng A 2016;662:443–55. https://doi.org/10.1016/j.msea.2016.03.092.
[13] Fedoseeva A, Dudova N, Glatzel U, Kaibyshev R. Effect of W on tempering behaviour of a 3 %Co modified P92 steel. J Mater Sci 2016;51:9424–39. https://doi.org/10.1007/s10853-016-0188-x.
[14] Kipelova A, Belyakov A, Kaibyshev R. Laves phase evolution in a modified P911 heat resistant steel during creep at 923K. Mater Sci Eng A 2012;532:71–7. https://doi.org/10.1016/j.msea.2011.10.064.
[15] Isik MI, Kostka A, Yardley VA, Pradeep KG, Duarte MJ, Choi PP, et al. The nucleation of Mo-rich Laves phase particles adjacent to M 23 C 6 micrograin boundary carbides in 12% Cr tempered martensite ferritic steels. Acta Mater 2015;90:94–104. https://doi.org/10.1016/j.actamat.2015.01.027.
[16] Mishnev R, Dudova N, Kaibyshev R. Low cycle fatigue behavior of a 10Cr–2W–Mo–3Co–NbV steel. Int J Fatigue 2016;83:344–55. https://doi.org/10.1016/j.ijfatigue.2015.11.008.
[17] Guguloth K, Sivaprasad S, Chakrabarti D, Tarafder S. Low-cyclic fatigue behavior of modified 9Cr–1Mo steel at elevated temperature. Mater Sci Eng A 2014;604:196–206. https://doi.org/10.1016/j.msea.2014.02.076.
[18] Golański G, Mroziński S. Low cycle fatigue and cyclic softening behaviour of martensitic cast steel. Eng Failure Analysis 2013;35:692–702. https://doi.org/10.1016/j.engfailanal.2013.06.019.
[19] Verma P, Santhi Srinivas NC, Singh V. Low Cycle Fatigue Behaviour of Modified 9Cr–1Mo Steel at 600 °C. Trans Indian Inst Metals 2016;69:331–5. https://doi.org/10.1007/s12666-015-0782-7.
[20] Mariappan K, Shankar V, Sandhya R, Prasad Reddy GV, Mathew MD. Dynamic strain aging behavior of modified 9Cr–1Mo and reduced activation ferritic martensitic steels under low cycle fatigue. J Nucl Mater 2013;435:207–13. https://doi.org/10.1016/j.jnucmat.2012.12.049.
[21] Fournier B, Dalle F, Sauzay M, Longour J, Salvi M, Caës C, et al. Comparison of various 9–12%Cr steels under fatigue and creep-fatigue loadings at high temperature. Mater Sci Eng A 2011;528:6934–45. https://doi.org/10.1016/j.msea.2011.05.046.
[22] Nagesha A, Kannan R, Srinivasan VS, Sandhya R, Choudhary BK, Laha K. Dynamic strain aging and oxidation effects on the thermomechanical fatigue deformation of reduced activation ferritic-martensitic steel. Metall Mater Trans A 2016;47:1110–27. https://doi.org/10.1007/s11661-015-3293-6.
[23] Fournier B, Sauzay M, Pineau A. Micromechanical model of the high temperature cyclic behavior of 9–12%Cr martensitic steels. Int J Plasticity 2011;27:1803–16. https://doi.org/10.1016/j.ijplas.2011.05.007.
[24] Mroziński S, Egner H, Piotrowski M. Effects of fatigue testing on low-cycle properties of P91 steel. Int J Fatigue 2019;120:65–72. https://doi.org/10.1016/j.ijfatigue.2018.11.001.
[25] Kim DW, Kim SS. Contribution of microstructure and slip system to cyclic softening of 9wt.%Cr steel. Int J Fatigue 2012;36:24–9. https://doi.org/10.1016/j.ijfatigue.2011.09.004.
[26] Wang X, Zhang W, Ni J, Zhang T, Gong J, Wahab MA. Quantitative description between pre-fatigue damage and residual tensile properties of P92 steel. Mater Sci Eng A 2019;744:415–25. https://doi.org/10.1016/j.msea.2018.12.029.
[27] Giordana MF, Giroux P-F, Alvarez-Armas I, Sauzay M, Armas A, Kruml T.

Microstructure evolution during cyclic tests on EUROFER 97 at room temperature. TEM observation and modelling. Mater Sci Eng A 2012;550:103–11. https://doi.org/10.1016/j.msea.2012.04.038.
[28] Hu X, Huang L, Yan W, Wang W, Sha W, Shan Y, et al. Low cycle fatigue properties of CLAM steel at 823 K. Mater Sci Eng A 2014;613:404–13. https://doi.org/10.1016/j.msea.2014.06.069.
[29] Tabuchi M, Hongo H, Abe F. Creep strength of dissimilar welded joints using high B-9Cr steel for advanced USC boiler. Metall Mater Trans A 2014;45:5068–75. https://doi.org/10.1007/s11661-014-2471-2.
[30] Mishnev R, Dudova N, Kaibyshev R. Effect of the strain rate on the low cycle fatigue behavior of a 10Cr-2W-Mo-3Co-NbV steel at 650 °C. Int J Fatigue 2017;100:113–25. https://doi.org/10.1016/j.ijfatigue.2017.03.025.
[31] Mishnev R, Dudova N, Kaibyshev R. Low cycle fatigue behavior of a 10% Cr martensitic steel at 600°C. ISIJ Int 2015;55:2469–76. https://doi.org/10.2355/isijinternational.ISIJINT-2015-336.
[32] Mishnev R, Dudova N, Kaibyshev R. Microstructure evolution during LCF of a 10%Cr Steel at room temperature. Mater Sci Forum 2016;879:1311–6. https://doi.org/10.4028/www.scientific.net/MSF.879.1311.
[33] Aghajani A, Somsen Ch, Eggeler G. On the effect of long-term creep on the microstructure of a 12% chromium tempered martensite ferritic steel. Acta Mater 2009;57:5093–106. https://doi.org/10.1016/j.actamat.2009.07.010.
[34] Masuyama F. Hardness model for creep-life assessment of high-strength martensitic steels. Mater Sci Eng A 2009;510–511:154–7. https://doi.org/10.1016/j.msea.2008.04.133.
[35] Maruyama K, Sawada K, Koike J-I. Strengthening mechanisms of creep resistant tempered martensitic steel. ISIJ Int 2001;41:641–53.
[36] Dudova N, Mishnev R, Kaibyshev R. Creep behavior of a 10%Cr heat-resistant martensitic steel with low nitrogen and high boron contents at 650 °C. Mater Sci Eng A 2019;766:138353. https://doi.org/10.1016/j.msea.2019.138353.
[37] Hirsch PB, Nicholson RB, Howie A, Pashley DW, Whelan MJ. Electron microscopy of thin crystals. London: Butterworths; 1965. p. 549.
[38] J.P. Hirth, J. Lothe, Theory of dislocations, 1992.
[39] Dudko V, Belyakov A, Kaibyshev R. Evolution of lath substructure and internal stresses in a 9% Cr steel during creep. ISIJ Int 2017;57:540–9. https://doi.org/10.2355/isijinternational.ISIJINT-2016-334.
[40] Mitsuhara M, Yamasaki S, Miake M, Nakashima H, Nishida M, Kusumoto J, et al. Creep strengthening by lath boundaries in 9Cr ferritic heat-resistant steel. Phil Mag Letters 2016;96:76–83. https://doi.org/10.1080/09500839.2016.1154200.